

## PHASE EQUILIBRIA OF THE Al-Co-Er SYSTEM AT 400°C AND 600°C

L.-H. Zheng, L.-G. Zhang \*, F.-Y. Zhao, L.-B. Liu, D. Wang, C.-J. Wu

School of Materials Science and Engineering, Central South University, Changsha, China

(Received 17 March 2021; accepted 14 June 2021)

### Abstract

The 400°C and 600°C isothermal sections of the Al-Co-Er system were studied assisted with X-ray diffraction (XRD), scanning electron microscopy (SEM), and electron probe microanalysis (EPMA) techniques. 18 three-phase fields were identified in the 400°C isothermal section. The maximum solid solubilities of Al in  $Co_3Er$  and  $Co_2Er$  were 13.93 at.%, and 16.13 at.%, respectively whereas the maximum solid solubilities of Co in  $Al_2Er$ ,  $Al_2Er_3$  and  $AlEr_2$  were 6.93 at.%, 6.65 at.%, and 6.49 at.%, respectively. The solid solution range of  $\lambda$  is from 22.22 at.% Al to 44.44 at.% Al while the 600°C isothermal section included 20 three-phase fields. The maximum solid solubilities of Al in  $Co_{17}Er_2$  and  $Co_7Er_2$  were 10.17 at.% and 10.24 at.%, respectively. The maximum solid solubilities of Co in  $Al_2Er$  and  $Al_2Er_3$  were 3.63 at.% and 2.01 at.%, respectively.

**Keywords:** Phase Equilibria; Al-Co-Er; Aluminum alloys

### 1. Introduction

Since Alfred Wilm [1-2] discovered age hardening in 1901, the development of high-strength Al alloys has gained much attention globally. Materials scientists often improve the strength of aluminum alloys by controlling the defects that prevent dislocation movement; however, this reinforcement effect cannot be expanded indefinitely [3-4].

Recent studies have shown that amorphization is also an effective method for improving the strength of Al alloy materials [5-7]. A bulk aluminum alloy with a record-high yield strength of 1.7GPa and Young's modulus of 120GPa have been designed based on the absence of grain boundaries and dislocations in the amorphous structure [8]. Therefore, the development of Al alloys with good amorphous-forming ability has become the key to designing high-strength Al alloys. However, the practical application of Al-based amorphous alloys has been greatly limited by the low glass-forming ability (GFA) of the alloys. In recent years, Al-TM-RE (TM: transition metals, RE: rare-earth elements) alloy systems [9-10], which mainly include Al-Cu-RE, Al-Co-RE, Al-Ni-RE, and Al-Fe-RE, have become a research focus owing to their good GFA and wide amorphous-forming range [11-12].

Reliable phase diagram information of the Al-TM-RE-related systems is indispensable for establishing accurate phase-diagram thermodynamic databases; these databases can in turn be used to predict the thermal stability of nanostructures and the

GFA for the design and fabrication of these intermetallic alloys [13-16].

The phase diagrams of the three binary systems Al-Co, Al-Er, and Co-Er have been investigated in the literature. In 1902, Guillet [17] studied the Al-Co phase diagram for the first time. Subsequently, Gwyer [18], Panteleimonov [19], and McAister [20] successively studied the Al-Co system and established the thermodynamic database. In 2013, Stein et al. [21] systematically analyzed the previous work and reevaluated the Al-Co binary system phase diagram based on the work by Dupin and Ansara [22] on the controversies about the Al-Co system. There are few studies on the Al-Er phase diagram, mainly based on the works by Buschow [23] in 1965 and Cacciamani [24] in 2002. In 1971, Buschow et al. [25] first studied the Co-Er binary system. In 1993, Okamoto and Massalski [26] recalculated and constructed the phase diagram of the Co-Er binary system according to the crystallographic data provided in Pearson's Handbook. In 1993, Wu et al. [27] reevaluated the phase diagram of the Co-Er binary system evaluated by Okamoto and Massalski [28]. In 2009, Wang et al. [29] thermodynamically assessed the Co-Er binary system on the basis of the experimental data on the thermodynamic properties and phase equilibria. The authors found that the calculated results agreed with the experimental data.

Crystal structures of phases in the Al-Co-Er ternary system are listed in Table 1, [20, 30-35]; however, the experimental phase-equilibrium

\*Corresponding author: ligangzhang@csu.edu.cn



information on the Al–Co–Er system is still lacking [36–45], and further experiments are needed to support thermodynamic optimization calculations. Therefore, in the current study, the phase equilibria at 400°C and 600°C in the Al–Co–Er system were investigated via scanning electron microscopy (SEM), electron probe microanalysis (EPMA), and X-ray diffraction (XRD).

## 2. Experimental

More than 70 alloy samples were prepared for the determination of the isothermal sections of the Al–

Co–Er ternary system at 400°C and 600°C. The raw materials, Al, Co, and Er (99.99% purity), supplied by China Materials Technology Co., Ltd., were smelted to obtain the experimental alloy samples. The weight of each sample was about 6 g. The composition of each sample was designed based on the existing phase diagram information, and the amount of each starting material was obtained by weighing with an analytical balance. The samples were arc-smelted in a vacuum consumable electrode arc furnace under an argon atmosphere in a water-cooled copper crucible, and the alloyed samples were smelted together with Ti as an

**Table 1.** The intermetallic compounds reported in the literature for the Al-Co-Er system along with crystal structure data

Phase	Structure type	Space group	SG No.	Lattice parameters/Å			$\beta$	$\gamma$	Ref.
				a	b	c			
$\lambda$ -Al <sub>4</sub> Co <sub>2</sub> Er <sub>3</sub>	MgZn <sub>2</sub>	P6 <sub>3</sub> /mmc	194	5.399		8.599		120°	[29]
$\lambda$ -AlCoEr	MgZn <sub>2</sub>	P6 <sub>3</sub> /mmc	194	5.299		8.475		120°	[30]
Al <sub>13</sub> Co <sub>53</sub> Er <sub>34</sub>	Cu <sub>2</sub> Mg	Fd-3m	227	7.380					[29]
AlCo <sub>3</sub> Er <sub>2</sub>	Cu <sub>2</sub> Mg	Fd-3m	227	7.272					[31]
$\tau_2$ -Al <sub>9</sub> Co <sub>3</sub> Er <sub>2</sub>	Al <sub>9</sub> Co <sub>3</sub> Y <sub>2</sub>	Cmcm	63	12.738	7.509	9.378			[32]
$\tau_5$ -AlCo <sub>2</sub> Er <sub>2</sub>	W2CoB2	Immm	71	4.042	5.436	8.327			[33]
$\tau_8$ -Al <sub>3</sub> CoEr <sub>2</sub>	Cu <sub>2</sub> Mg	Fd-3m	227	7.681					[31]
$\alpha$ -Co	Cu	Fd-3m	227	3.563					[29]
$\epsilon$ -Co	Mg	P6 <sub>3</sub> /mmc	194	2.506		4.069			[29]
Al <sub>9</sub> Co <sub>2</sub>	Al <sub>9</sub> Co <sub>2</sub>	P2 <sub>1</sub> /a	14	8.565	6.290	6.213	94.76°		[34]
Al <sub>13</sub> Co <sub>4</sub>	Al <sub>13</sub> Co <sub>4</sub>	Cm	8	15.183	8.122	12.340	107.90°		[29]
Al <sub>13</sub> Co <sub>4</sub>	Al <sub>13</sub> Co <sub>4</sub>	Pmn2 <sub>1</sub>	31	8.158	12.342	14.452			[29]
Al <sub>3</sub> Co	T <sup>2</sup> -Al <sub>13</sub> Co <sub>4</sub>			12.5	8.1	14.6			[29]
Al <sub>5</sub> Co <sub>2</sub>	Al <sub>5</sub> Co <sub>2</sub>	P6 <sub>3</sub> /mmc	194	7.656		7.593			[29]
AlCo	CsCl	Pm-3m	221	2.863					[29]
Al <sub>87</sub> Al <sub>13</sub>	Cu	Fm-3m	227	3.568					[29]
Al <sub>3</sub> Er	Cu <sub>3</sub> Au	Pm-3m	221	4.215					[29]
Al <sub>2</sub> Er	Cu <sub>2</sub> Mg	Fm-3m	227	7.775					[29]
AlEr	AlDy	Pbcm	57	5.801	11.272	5.570			[29]
Al <sub>2</sub> Er <sub>3</sub>	Al <sub>2</sub> Gd <sub>3</sub>	P4 <sub>2</sub> nm	102	8.123		7.484		120°	[29]
AlEr <sub>2</sub>	SiCo <sub>3</sub>	Pnma	62	6.516	5.015	9.279			[29]
CoEr <sub>3</sub>	CFe <sub>3</sub>	Pnma	62	6.902	9.191	6.189			[29]
Co <sub>7</sub> Er <sub>12</sub>	Co <sub>7</sub> Ho <sub>12</sub>	P2 <sub>1</sub> /c	14	8.305	11.165	13.825	138.7°	120°	[29]
Co <sub>3</sub> Er <sub>4</sub>	Co <sub>3</sub> Ho <sub>4</sub>	P6 <sub>3</sub> /m	176	11.32		3.967			[20]
Co <sub>2</sub> Er	Cu <sub>2</sub> Mg	Fd-3m	227	7.155				120°	[29]
Co <sub>3</sub> Er	Be <sub>3</sub> Nb	R-3m	166	4.978		24.258		120°	[29]
Co <sub>7</sub> Er <sub>2</sub>	Co <sub>7</sub> Er <sub>2</sub>	R-3m	166	4.973		36.111		120°	[29]
Co <sub>5</sub> Er	Cu <sub>5</sub> Ca	P6/mmm	191	4.870		4.002		120°	[29]
Co <sub>17</sub> Er <sub>2</sub>	Ni <sub>17</sub> Th <sub>2</sub>	P6 <sub>3</sub> /mmc	194	8.313		8.131		120°	[29]



oxygen getter to prevent oxidation during smelting. To ensure the uniformity of the samples, each button sample was turned and re-melted at least three times during smelting, with the weight loss not exceeding 1%. The obtained button alloy samples were sealed in silica capsules backfilled with high-purity argon to resist oxidization and then annealed in a tube furnace at 400°C for 2880 hours and 600°C for 2160 hours. Afterward, the alloy samples were immediately immersed in ice water to quench and cool to room temperature.

The microstructures of these alloy samples were investigated via EPMA (JEOL JXA-8530F) after the samples were polished. The total mass of all the elements in each phase ranged from 97% to 103%, and the standard deviation of the measured concentration was  $\pm 0.5$  at.%. The phases in the alloy samples were identified using a Rigaku D-max/2500 X-ray diffractometer operated at 40 kV and 200 mA. The phase-identification results were analyzed using the Jade 6.0 program, and the diffraction patterns were obtained.

### 3. Results and Discussion

#### 3.1. Isothermal Section at 400°C

The nominal chemical compositions of 35 alloy samples and the chemical compositions of each individual phase at 400°C obtained via EPMA are summarized in Table 2.

Figures 1(a) and 1(b) display the microstructure and phase composition of alloy #A1, respectively; the alloy contained  $\text{Al}_3\text{Co}$  (dark phase),  $\text{Al}_{19}\text{Co}_6\text{Er}_2$  (bright phase), and  $\text{Al}_5\text{Co}_2$  (gray phase). Figure 1(c) shows the microstructure of alloy #A2, which contained  $\text{Al}_3\text{Er}$  (light gray phase),  $\text{Al}_9\text{Co}_2$  (gray phase), and Al (dark phase), based on the XRD result in Fig. 1(d). According to Fig. 1(e, f), alloy #A4 was located in a three-phase equilibrium field:  $\text{Al}_2\text{Er}+\text{Al}_2\text{Er}_3+\text{AlEr}$ , while alloy #A5 was located in another three-phase area:  $\text{Al}_5\text{Co}_2+\text{AlCo}+\text{Al}_9\text{Co}_3\text{Er}_2$ , based on the EPMA and XRD results shown in Fig. 1(g, h). Meanwhile, alloy #A8 was in the same area as alloy #A5.

As shown in Fig. 2(a), alloy #A7 comprised  $\text{Al}_9\text{Co}_3\text{Er}_2$  (dark-gray phase),  $\text{Al}_3\text{Er}$  (light-gray phase), and  $\text{Al}_2\text{Er}$  (the brightest phase). From the microstructure results and XRD pattern analyses, it can be judged that the alloys #A3, #A10, and #A19 were located in the same three-phase equilibrium field:  $\text{Al}_3\text{Er}+\text{Al}_{19}\text{Co}_6\text{Er}_2+\text{Al}_9\text{Co}_2$  (Fig. 2c). Figure 2(e) shows the three-phase microstructure of

Table 2. Equilibrium compositions at 400°C measured with EPMA method

No.	Alloy/at.%			Phase equilibrium Phase 1/Phase 2/Phase 3	Phase composition/at.%					
	Al	Co	Er		Phase 1		Phase 2		Phase 3	
					Al	Co	Al	Co	Al	Co
#A1	70	20	10	$\text{Al}_{19}\text{Co}_6\text{Er}_2/\text{Al}_5\text{Co}_2/\text{Al}_3\text{Co}$	70.78	22.31	71.51	28.30	74.64	25.20
#A2	85	5	10	$\text{Al}/\text{Al}_3\text{Er}/\text{Al}_9\text{Co}_2$	99.79	0.10	74.80	1.94	82.45	17.22
#A3	77.5	20	2.5	$\text{Al}_9\text{Co}_2/\text{Al}_{19}\text{Co}_6\text{Er}_2/\text{Al}_3\text{Er}$	82.45	17.06	71.81	20.99	74.03	3.42
#A4	55	5	40	$\text{Al}_2\text{Er}/\text{Al}_2\text{Er}_3/\text{AlEr}$	61.17	6.93	35.02	6.65	48.40	4.43
#A5	72.5	25	2.5	$\text{Al}_5\text{Co}_2/\text{AlCo}/\text{Al}_9\text{Co}_3\text{Er}_2$	71.95	27.78	52.20	47.05	64.13	21.96
#A6	50	30	20	$\text{AlCo}/\text{Al}_{12}\text{Co}_4\text{Er}_3/\lambda$	50.17	49.28	54.12	29.90	44.71	23.94
#A7	62.5	20	17.5	$\text{Al}_9\text{Co}_3\text{Er}_2/\text{Al}_3\text{Er}/\text{Al}_2\text{Er}$	66.56	19.30	74.09	3.10	67.72	1.43
#A8	65	30	5	$\text{Al}_5\text{Co}_2/\text{AlCo}/\text{Al}_9\text{Co}_3\text{Er}_2$	71.68	27.80	52.99	46.67	64.09	22.41
#A9	55	30	15	$\text{AlCo}/\text{Al}_{12}\text{Co}_4\text{Er}_3/\lambda$	50.31	49.07	56.28	28.34	44.36	23.68

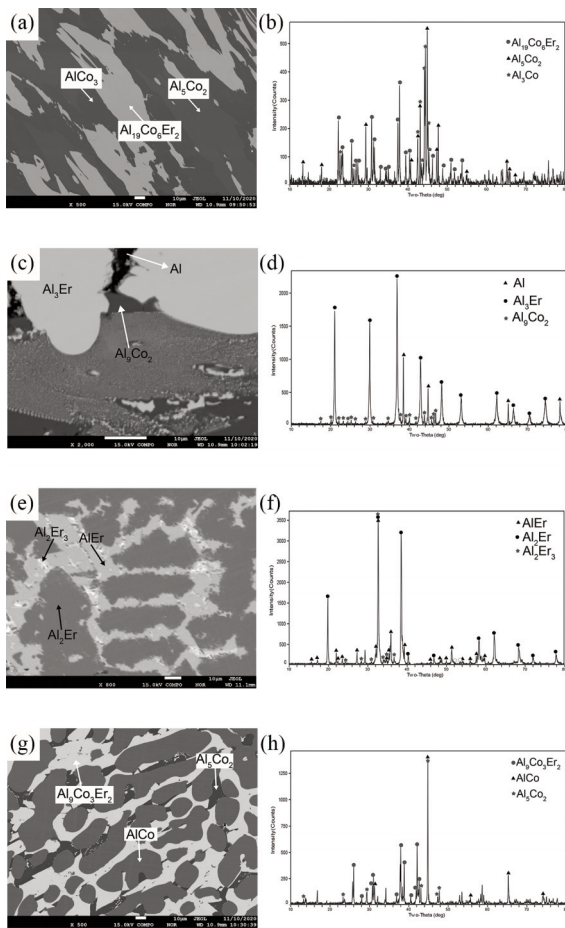
table continuous on the next page



table continuous from the previous page

#A10	70	25	5	$\text{Al}_3\text{Er}/\text{Al}_{19}\text{Co}_6\text{Er}_2/\text{Al}_9\text{Co}_2$	74.45	4.15	71.30	21.56	80.91	14.59
#A11	55	5	40	$\text{Al}_2\text{Er}/\text{Al}_{12}\text{Co}_4\text{Er}_3/\text{Al}_2\text{Er}$	63.72	5.32	62.51	21.99	57.34	22.36
#A12	70	15	15	$\text{Al}_3\text{Er}/\text{Al}_{19}\text{Co}_6\text{Er}_2/\text{Al}_9\text{Co}_3\text{Er}_2$	74.79	2.21	72.33	20.42	65.61	20.78
#A13	60	10	30	$\text{Al}_2\text{Er}/\text{Al}_{12}\text{Co}_4\text{Er}_3/\text{Al}_2\text{Er}$	63.22	4.89	61.94	22.00	54.62	24.58
#A14	75	15	10	$\text{Al}_9\text{Co}_2/\text{Al}_{19}\text{Co}_6\text{Er}_2/\text{Al}_{13}\text{Co}_4$	82.26	17.35	71.74	21.30	76.37	23.15
#A15	45	40	15	$\text{Al}_9\text{Co}_3\text{Er}_2/\text{Al}_{19}\text{Co}_6\text{Er}_2/\text{Al}_5\text{Co}_2$	64.20	22.08	71.06	21.62	71.97	27.56
#A16	70	5	25	$\text{Al}_3\text{Er}/\text{Al}_{19}\text{Co}_6\text{Er}_2/\text{Al}_9\text{Co}_3\text{Er}_2$	74.02	3.28	72.34	20.98	65.76	20.78
#A17	75	20	5	$\text{Al}_9\text{Co}_2/\text{Al}_{19}\text{Co}_6\text{Er}_2/\text{Al}_{13}\text{Co}_4$	82.05	17.69	71.15	21.87	76.04	23.82
#A18	60	25	15	$\text{AlCo}/\lambda/\text{Al}_{12}\text{Co}_4\text{Er}_3$	52.15	47.09	56.53	23.62	64.58	21.37
#A19	75	22.5	2.5	$\text{Al}_3\text{Er}/\text{Al}_{19}\text{Co}_6\text{Er}_2/\text{Al}_9\text{Co}_2$	72.04	5.19	70.36	21.28	81.10	13.43
#A20	55	5	40	$\text{Co}_2\text{Er}/\lambda/\text{AlCo}_2\text{Er}$	16.13	51.25	21.45	44.56	25.54	47.28
#A21	35	5	60	$\lambda/\text{Al}_3\text{Co}_3\text{Er}_{14}/\text{AlEr}_2$	45.74	15.18	17.61	16.39	29.42	6.49
#A22	40	35	25	$\text{AlCo}/\lambda$	50.81	47.61	43.72	26.70		
#A23	20	75	5	$\text{Al}_3\text{Co}_3\text{Er}_{14}/\text{AlCo}_2\text{Er}_6/\text{AlCo}_2\text{Er}_2$	5.52	15.16	15.50	19.48	15.94	33.58
#A24	50	30	20	$\text{AlCo}/\lambda$	60.09	32.47	45.23	22.12		
#A25	20	10	70	$\lambda/\text{Al}_2\text{Er}_3/\text{AlEr}_2$	45.74	18.51	34.97	4.31	30.12	6.37
#A26	30	60	10	$\text{AlCo}_2\text{Er}_2/\lambda/\text{Al}_3\text{Co}_3\text{Er}_{14}$	16.78	29.21	36.99	22.70	15.75	20.81
#A27	20	60	20	$\text{Er}/\text{AlEr}_2/\text{Al}_3\text{Co}_3\text{Er}_{14}$	54.15	9.66	33.24	3.98	0.00	5.82
#A28	35	5	60	$\lambda/\text{Al}_2\text{Er}_3$	27.25	45.15	33.29	4.22		
#A29	25	30	45	$\text{AlEr}_2/\text{Al}_3\text{Co}_3\text{Er}_{14}$	12.03	11.11	33.18	4.39	25.94	29.44
#A30	25	65	10	$\text{Co}_3\text{Er}/\text{AlCo}_2\text{Er}/\text{AlCo}$	10.36	65.35	30.89	52.92	49.72	50.02
#A31	40	35	25	$\text{AlCo}/\lambda/\text{AlCo}_2\text{Er}$	50.96	40.68	30.93	44.82	26.32	48.20
#A32	40	50	10	$\text{Co}_3\text{Er}/\text{AlCo}_2\text{Er}/\text{AlCo}$	51.44	40.89	26.82	48.66	13.93	61.72
#A33		47.5	30	$\lambda/\text{AlCo}_2\text{Er}_2$	23.03	30.95	22.78	39.48		
#A34	20	75	5	$\text{AlCo}_2\text{Er}/\text{AlCo}$	21.26	56.88	46.32	43.42		
#A35	40	40	20	$\text{AlCo}/\lambda$	44.76	47.56	30.56	30.26		





**Figure 1.** EPMA images and XRD results of 400°C-annealed alloys containing three phases after quenching: (a) microstructure of alloy #A1; (b) XRD result of alloy #A1; (c) microstructure of alloy #A2; (d) XRD result of alloy #A2; (e) microstructure of alloy #A4; (f) XRD result of alloy #A4; (g) microstructure of alloy #A5; (h) XRD result of alloy #A5

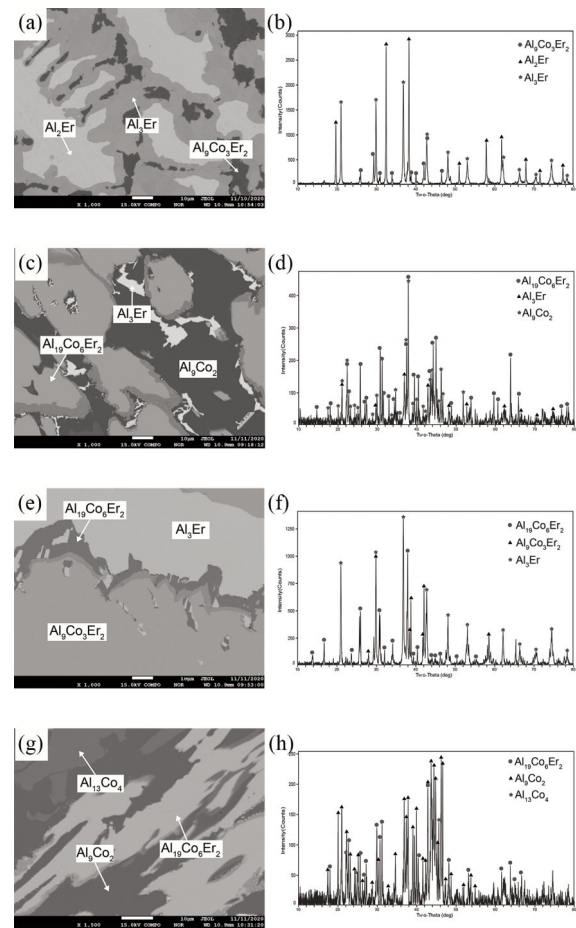


**Figure 2.** EPMA images and XRD results of 400°C-annealed alloys containing three phases after quenching: (a) microstructure of alloy #A7; (b) XRD result of alloy #A7; (c) microstructure of alloy #A10; (d) XRD result of alloy #A10; (e) microstructure of alloy #A12; (f) XRD result of alloy #A12; (g) microstructure of alloy #A14; (h) XRD result of alloy #A14

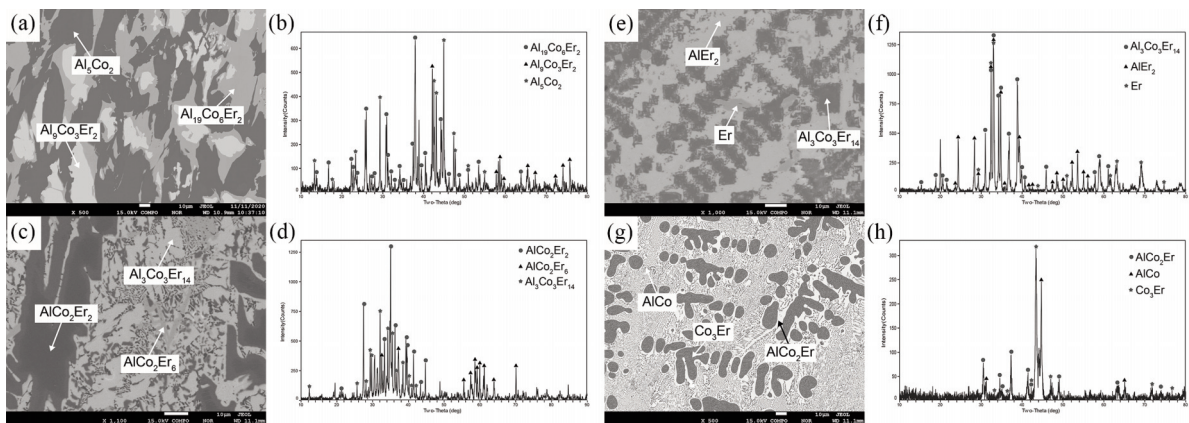


**Figure 3.** EPMA images and XRD results of 400°C-annealed alloys containing three phases after quenching: (a) microstructure of alloy #A15; (b) XRD result of alloy #A15; (c) microstructure of alloy #A23; (d) XRD result of alloy #A23; (e) microstructure of alloy #A27; (f) XRD result of alloy #A27; (g) microstructure of alloy #A30; (h) XRD result of alloy #A30

$\text{Al}_3\text{Er}+\text{Al}_{19}\text{Co}_6\text{Er}_2+\text{Al}_9\text{Co}_3\text{Er}_2$  of alloy #A12, and the XRD result is presented in Fig. 2(f). Alloys #A14 and #A17 also contained the same three phases:  $\text{Al}_{13}\text{Co}_4+\text{Al}_{19}\text{Co}_6\text{Er}_2+\text{Al}_9\text{Co}_2$  (Fig. 2g).

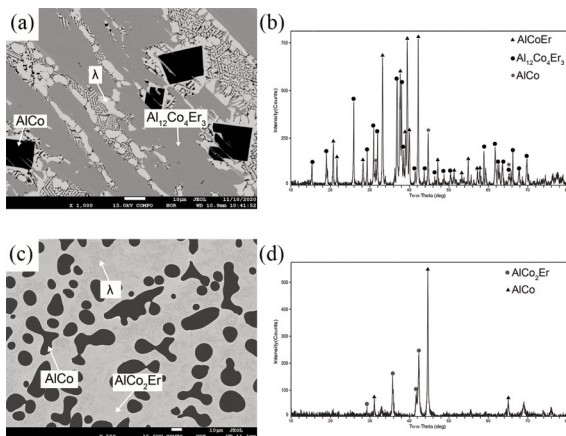
Alloy #A15 was composed of  $\text{Al}_9\text{Co}_3\text{Er}_2$ ,  $\text{Al}_{19}\text{Co}_6\text{Er}_2$ , and  $\text{Al}_5\text{Co}_2$  (Fig. 3a). The existence of the three-phase field  $\text{Al}_3\text{Co}_3\text{Er}_{14}+\text{AlCo}_2\text{Er}_6+\text{AlCo}_2\text{Er}_2$  and its location were also established based on the EPMA and XRD data of alloy #A23 (Fig. 3c and d). Meanwhile, alloy #A27 was located in the  $\text{Al}_3\text{Co}_3\text{Er}_{14}+\text{AlEr}_2+(\text{Er})$  three-phase area (Fig. 3e). Figure 3(g) displays the EPMA micrograph of alloy #A30, which features a three-phase area of  $\text{Co}_3\text{Er}+\text{AlCo}_2\text{Er}+\text{AlCo}$ , that agrees with the XRD result in Fig. 3(h). Alloy #A32 showed the same result as alloy #A30.

Figure 4(a) shows the microstructure of alloy #A6, which is comprised of AlCo (dark phase),  $\text{Al}_{12}\text{Co}_4\text{Er}_3$

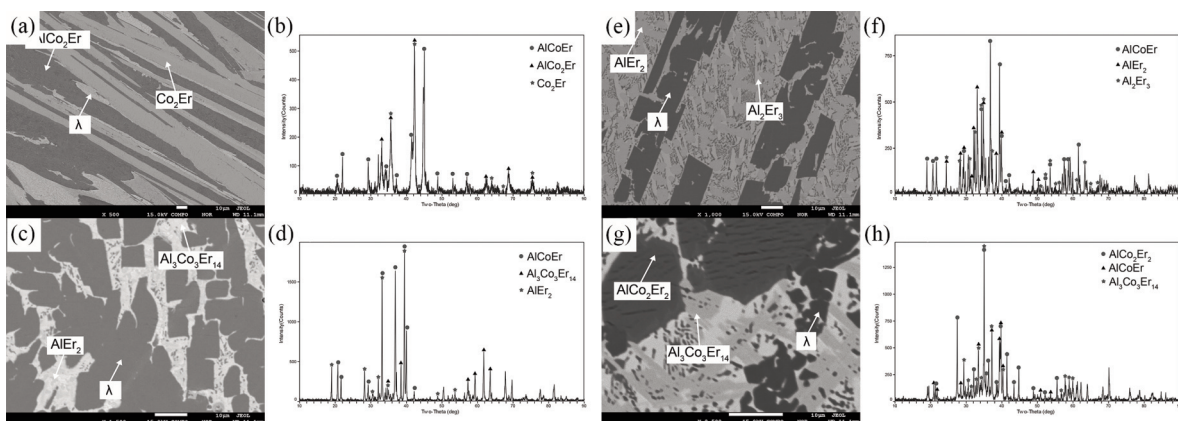
(gray phase), and  $\lambda$  (bright phase). The same result was obtained for alloys #A9 and #A18. Among the three phases, phase  $\lambda$  was confirmed to be a solid solution including AlCoEr and  $\text{Al}_4\text{Co}_2\text{Er}_3$ , and it also existed in alloys #A31 (Fig. 4c), #A20 (Fig. 5a), #A21 (Fig. 5c), #A25 (Fig. 5e), and #A26 (Fig. 5g). As presented in Fig. 4(c, d) and Fig. 5, these five alloy samples exhibited the following three-phase fields:  $\text{AlCo}+\lambda+\text{AlCo}_2\text{Er}$ ,  $\text{Co}_2\text{Er}+\lambda+\text{AlCo}_2\text{Er}$ ,  $\lambda+\text{Al}_3\text{Co}_3\text{Er}_{14}+\text{AlEr}_2$ ,  $\lambda+\text{AlEr}_2+\text{Al}_2\text{Er}_3$ , and  $\text{AlCo}_2\text{Er}_2+\lambda+\text{Al}_3\text{Co}_3\text{Er}_{14}$ , respectively.

Figure 6 shows the EPMA micrographs and XRD patterns of alloys #A22, #A28, and #A33, which featured the following two-phase equilibrium fields:  $\text{AlCo}+\lambda$ ,  $\text{Al}_2\text{Er}_3+\lambda$ , and  $\text{AlCo}_2\text{Er}_2+\lambda$ , respectively. Phase  $\lambda$  occurred in the three fields, as confirmed by the occurrence of solid solubility. Likewise, Fig. 7 presents the experimental results of other two-phase fields:  $\text{Al}_3\text{Er}+\text{Al}_{12}\text{Co}_4\text{Er}_3$ ,  $\text{AlEr}_2+\text{Al}_3\text{Co}_3\text{Er}_{14}$ , and  $\text{AlCo}_2\text{Er}+\text{AlCo}$ .

According to the EPMA data and XRD patterns in Table 2, the isothermal section of the Al–Co–Er ternary system at 400°C was established (Fig. 8). As shown in Fig. 8, eight ternary intermediate compounds were detected in the Al–Co–Er system at 400°C:  $\text{Al}_{19}\text{Co}_6\text{Er}_2$ ,  $\text{Al}_9\text{Co}_3\text{Er}_2$ ,  $\text{Al}_{12}\text{Co}_4\text{Er}_3$ ,  $\lambda$  (solid solution including AlCoEr and  $\text{Al}_4\text{Co}_2\text{Er}_3$ ),  $\text{AlCo}_2\text{Er}$ ,  $\text{AlCo}_2\text{Er}_2$ ,  $\text{AlCo}_2\text{Er}_6$ , and  $\text{Al}_3\text{Co}_3\text{Er}_{14}$ . Five of these ternary intermediate compounds ( $\text{Al}_{19}\text{Co}_6\text{Er}_2$ ,  $\text{Al}_{12}\text{Co}_4\text{Er}_3$ ,  $\text{AlCo}_2\text{Er}$ ,  $\text{AlCo}_2\text{Er}_6$ , and  $\text{Al}_3\text{Co}_3\text{Er}_{14}$ ) have not been previously reported. Although alloy samples of pure ternary intermediate compounds were not obtained, their existence can be proved by combining the EPMA data with the XRD results. The maximum solid solubilities of Al in  $\text{Co}_3\text{Er}$  and  $\text{Co}_2\text{Er}$  were 13.93 at.% and 16.13 at.%, respectively, whereas those of Co in  $\text{Al}_2\text{Er}$ ,  $\text{Al}_2\text{Er}_3$ , and  $\text{AlEr}_2$  were 6.93 at.%, 6.65 at.%, and 6.49 at.%, respectively. The solubility range



**Figure 4.** EPMA images and XRD results of 400°C-annealed alloys containing three phases after quenching: (a) microstructure of alloy #A6; (b) XRD result of alloy #A6; (c) microstructure of alloy #A31; (d) XRD result of alloy #A31



**Figure 5.** EPMA images and XRD results of 400°C-annealed alloys containing three phases after quenching: (a) microstructure of alloy #A20; (b) XRD result of alloy #A20; (c) microstructure of alloy #A21; (d) XRD result of alloy #A21; (e) microstructure of alloy #A25; (f) XRD result of alloy #A25; (g) microstructure of alloy #A26; (h) XRD result of alloy #A26

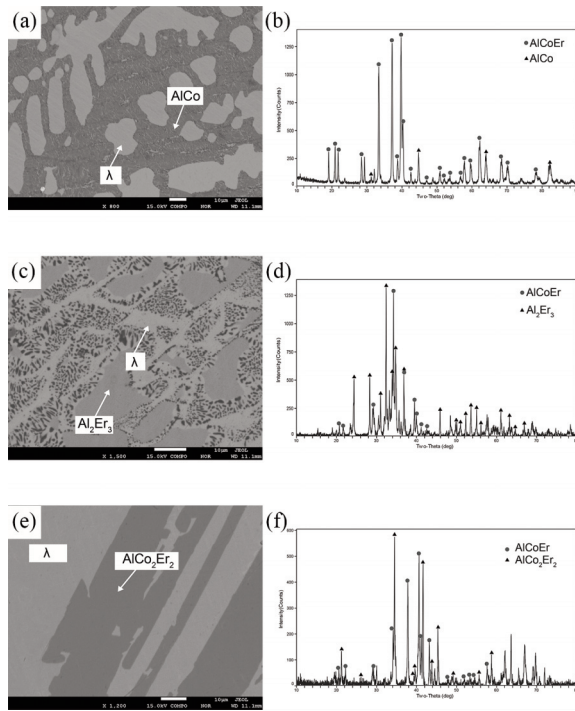


**Figure 6.** EPMA images and XRD results of 400°C-annealed alloys containing two phases after quenching: (a) microstructure of alloy #A22; (b) XRD result of alloy #A22; (c) microstructure of alloy #A28; (d) XRD result of alloy #A28; (e) microstructure of alloy #A33; (f) XRD result of alloy #A33

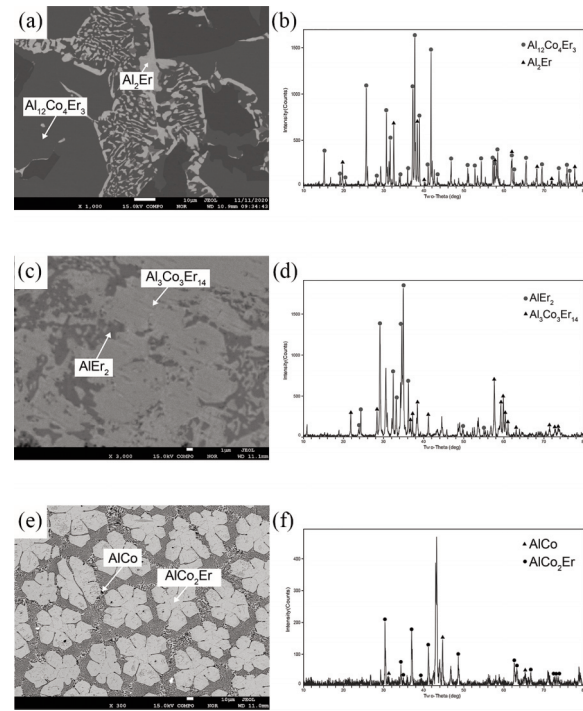


**Figure 7.** EPMA images and XRD results of 400°C-annealed alloys containing two phases after quenching: (a) microstructure of alloy #A11; (b) XRD result of alloy #A11; (c) microstructure of alloy #A29; (d) XRD result of alloy #A29; (e) microstructure of alloy #A34; (f) XRD result of alloy #A34

of AlCo was from 46.32 at.% Al to 52.15 at.% Al, and the solid solution range of  $\lambda$  was from 22.22 at.% Al to 44.44 at.% Al.

From the data analysis above, 18 three-phase equilibrium regions and 6 two-phase equilibrium regions were detected in the isothermal section of the

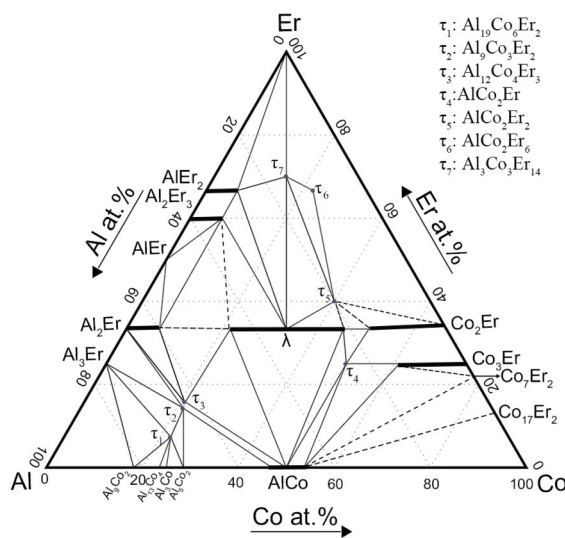


**Figure 8.** Isothermal section of Al-Co-Er system at 400°C

Al-Co-Er system at 400°C: (Al)+Al<sub>3</sub>Er+Al<sub>9</sub>Co<sub>2</sub>, Al<sub>2</sub>Er+Al<sub>2</sub>Er<sub>3</sub>+AlEr, Al<sub>19</sub>Co<sub>6</sub>Er<sub>2</sub>+Al<sub>5</sub>Co<sub>2</sub>+Al<sub>3</sub>Co, Al<sub>3</sub>Er+Al<sub>19</sub>Co<sub>6</sub>Er<sub>2</sub>+Al<sub>9</sub>Co<sub>2</sub>, Al<sub>9</sub>Co<sub>2</sub>+Al<sub>19</sub>Co<sub>6</sub>Er<sub>2</sub>+Al<sub>13</sub>Co<sub>4</sub>, Al<sub>5</sub>Co<sub>2</sub>+AlCo+Al<sub>9</sub>Co<sub>3</sub>Er<sub>2</sub>, Al<sub>9</sub>Co<sub>3</sub>Er<sub>2</sub>+Al<sub>3</sub>Er+Al<sub>2</sub>Er, Al<sub>3</sub>Er+Al<sub>19</sub>Co<sub>6</sub>Er<sub>2</sub>+Al<sub>9</sub>Co<sub>3</sub>Er<sub>2</sub>, Al<sub>9</sub>Co<sub>3</sub>Er<sub>2</sub>+Al<sub>19</sub>Co<sub>6</sub>Er<sub>2</sub>+Al<sub>5</sub>Co<sub>2</sub>, Al<sub>3</sub>Co<sub>3</sub>Er<sub>14</sub>+AlCo<sub>2</sub>Er<sub>6</sub>+AlCo<sub>2</sub>Er<sub>2</sub>, (Er)+AlEr<sub>2</sub>+Al<sub>3</sub>Co<sub>3</sub>Er<sub>14</sub>, Co<sub>3</sub>Er+AlCo<sub>2</sub>Er+AlCo, AlCo+Al<sub>12</sub>Co<sub>4</sub>Er<sub>3</sub>+ $\lambda$ , AlCo+ $\lambda$ +AlCo<sub>2</sub>Er, Co<sub>2</sub>Er+ $\lambda$ +AlCo<sub>2</sub>Er,  $\lambda$ +Al<sub>3</sub>Co<sub>3</sub>Er<sub>14</sub>+AlEr<sub>2</sub>,  $\lambda$ +Al<sub>2</sub>Er<sub>3</sub>+AlEr<sub>2</sub>, AlCo<sub>2</sub>Er<sub>2</sub>+ $\lambda$ +Al<sub>3</sub>Co<sub>3</sub>Er<sub>14</sub>, AlCo+ $\lambda$ , Al<sub>2</sub>Er<sub>3</sub>+ $\lambda$ , AlCo<sub>2</sub>Er<sub>2</sub>+ $\lambda$ , Al<sub>2</sub>Er+Al<sub>12</sub>Co<sub>4</sub>Er<sub>3</sub>, AlEr<sub>2</sub>+Al<sub>3</sub>Co<sub>3</sub>Er<sub>14</sub>, AlCo<sub>2</sub>Er+AlCo. Then, according to the determination of the phase equilibrium relationship, six undetected phase regions were obtained by prediction (shown by dashed lines in Fig. 8).

### 3.2. Isothermal Section at 600°C

According to the EPMA data and XRD patterns in Table 3, the isothermal section of the Al-Co-Er ternary system at 600°C was established (Fig. 13).

According to the data from in Table 3, the isothermal sections of Al-Co-Er system at 400°C and 600°C had 9 three-phase fields in common: (Al)+Al<sub>3</sub>Er+Al<sub>9</sub>Co<sub>2</sub>, Al<sub>2</sub>Er+Al<sub>2</sub>Er<sub>3</sub>+AlEr, Al<sub>3</sub>Er+Al<sub>19</sub>Co<sub>6</sub>Er<sub>2</sub>+Al<sub>9</sub>Co<sub>2</sub>, Al<sub>9</sub>Co<sub>2</sub>+Al<sub>19</sub>Co<sub>6</sub>Er<sub>2</sub>+Al<sub>13</sub>Co



$\text{Al}_5\text{Co}_2+\text{AlCo}+\text{Al}_9\text{Co}_3\text{Er}_2$ ,  $\text{Al}_9\text{Co}_3\text{Er}_2+\text{Al}_3\text{Er}+\text{Al}_2\text{Er}$ ,  $\text{Al}_3\text{Er}+\text{Al}_{19}\text{Co}_6\text{Er}_2+\text{Al}_9\text{Co}_3\text{Er}_2$ ,  $\text{Al}_9\text{Co}_3\text{Er}_2+\text{Al}_{19}\text{Co}_6\text{Er}_2+\text{Al}_5\text{Co}_2$ , and  $\text{AlCo}+\text{Al}_{12}\text{Co}_4\text{Er}_3+\lambda$ .

Furthermore, the EPMA micrographs and XRD

patterns of alloys #B5, #B14 and #B17 (Fig. 9) featured the following three-phase fields:  $\text{Al}_{19}\text{Co}_6\text{Er}_2+\text{Al}_9\text{Co}_2+\text{Al}_3\text{Co}$ ,  $\text{Al}_{12}\text{Co}_4\text{Er}_3+\text{Al}_9\text{Co}_3\text{Er}_2+\text{Al}_2\text{Er}$ , and  $\text{Al}_{12}\text{Co}_4\text{Er}_3+\text{Al}_9\text{Co}_3\text{Er}_2+\text{AlCo}$ , respectively.

**Table 3.** Equilibrium compositions at 600°C measured with EPMA method

No.	Alloy/at.%			Phase equilibrium Phase 1/Phase 2/Phase 3	Phase composition/at.%					
	Al	Co	Er		Phase 1		Phase 2		Phase 3	
					Al	Co	Al	Co	Al	Co
#B1	85	5	10	$\text{Al}/\text{Al}_9\text{Co}_2/\text{Al}_3\text{Er}$	99.76	0.17	82.59	17.41	76.73	1.34
#B2	77.5	20	2.5	$\text{Al}_9\text{Co}_2/\text{Al}_{13}\text{Co}_4/\text{Al}_{19}\text{Co}_6\text{Er}_2$	81.31	18.60	76.05	22.98	70.87	22.21
#B3	75	15	10	$\text{Al}_9\text{Co}_2/\text{Al}_{19}\text{Co}_6\text{Er}_2/\text{Al}_3\text{Er}$	81.95	18.5	70.59	22.41	75.15	4.02
#B4	75	20	5	$\text{Al}_9\text{Co}_2/\text{Al}_{19}\text{Co}_6\text{Er}_2/\text{Al}_3\text{Er}$	81.66	17.99	72.43	22.23	74.33	3.34
#B5	75	2.5	2.5	$\text{Al}_{19}\text{Co}_6\text{Er}_2/\text{Al}_9\text{Co}_2/\text{Al}_3\text{Co}$	72.70	21.10	81.75	18.25	75.62	24.38
#B6	72.5	25	2.5	$\text{Al}_5\text{Co}_2/\text{AlCo}/\text{Al}_9\text{Co}_3\text{Er}_2$	71.20	28.72	52.64	47.36	64.24	22.77
#B7	72.5	22.5	5	$\text{Al}_5\text{Co}_2/\text{Al}_{19}\text{Co}_6\text{Er}_2$	71.39	27.14	70.59	22.56		
#B8	70	25	5	$\text{Al}_5\text{Co}_2/\text{Al}_{19}\text{Co}_6\text{Er}_2/\text{Al}_9\text{Co}_3\text{Er}_2$	71.25	28.58	70.99	22.28	64.50	21.81
#B9	70	20	10	$\text{Al}_{19}\text{Co}_6\text{Er}_2/\text{Al}_9\text{Co}_3\text{Er}_2/\text{Al}_3\text{Er}$	70.86	21.67	64.43	21.61	75.02	2.00
#B10	70	15	15	$\text{Al}_{19}\text{Co}_6\text{Er}_2/\text{Al}_9\text{Co}_3\text{Er}_2/\text{Al}_3\text{Er}$	71.53	21.50	64.26	21.60	74.85	1.97
#B11	70	10	20	$\text{Al}_{19}\text{Co}_6\text{Er}_2/\text{Al}_9\text{Co}_3\text{Er}_2/\text{Al}_3\text{Er}$	72.86	19.89	65.50	20.76	75.54	1.79
#B12	70	5	25	$\text{Al}_{19}\text{Co}_6\text{Er}_2/\text{Al}_2\text{Er}/\text{Al}_3\text{Er}$	65.99	20.5	75.40	2.28	71.43	20.88
#B13	65	30	5	$\text{Al}_5\text{Co}_2/\text{AlCo}/\text{Al}_9\text{Co}_3\text{Er}_2$	69.24	30.13	50.94	47.78	63.46	22.65
#B14	62.5	20	17.5	$\text{Al}_9\text{Co}_3\text{Er}_2/\text{Al}_{12}\text{Co}_4\text{Er}_3/\text{Al}_2\text{Er}$	65.42	21.66	62.98	23.13	63.49	5.56

table continuous on the next page



table continuous from the previous page

#B15	60	25	15	$\text{Al}_{12}\text{Co}_4\text{Er}_3/\text{Al}_2\text{Er}$	61.32	23.25	62.70	4.82		
#B16	60	10	30	$\text{Al}_{12}\text{Co}_4\text{Er}_3/\text{Al}_9\text{Co}_3\text{Er}_2/\text{Al}_2\text{Er}$	60.79	23.50	55.41	24.50	62.01	6.72
#B17	55	30	15	$\text{AlCo}/\text{Al}_9\text{Co}_3\text{Er}_2/\text{Al}_{12}\text{Co}_4\text{Er}_3$	51.90	42.10	60.98	23.98	55.33	25.33
#B18	55	5	40	$\text{Al}_2\text{Er}/\text{AlEr}/\text{Al}_2\text{Er}_3$	63.54	3.63	47.79	1.56	36.46	2.01
#B19	50	30	20	$\text{Al}_{12}\text{Co}_4\text{Er}_3/\lambda/\text{AlCo}$	47.90	50.07	51.29	31.56	41.16	25.75
#B20	45	40	15	$\text{Al}_2\text{Er}_3/\text{Al}_2\text{Er}$	38.44	6.93	31.69	7.52		
#B21	40	35	25	$\text{AlCo}_2\text{Er}_6/\text{AlCo}_2\text{Er}_2/\text{Al}_5\text{Co}_4\text{Er}_{11}$	13.97	21.90	19.76	41.85	21.92	24.67
#B22	35	5	60	$\text{AlCo}/\text{Co}_{17}\text{Er}_2/\text{Co}_7\text{Er}_2$	45.65	50.29	10.17	80.47	28.81	71.19
#B23	30	60	10	$\text{AlCo}/\text{Co}_{17}\text{Er}_2$	43.52	56.46	22.70	65.97		
#B24	25	30	45	$\text{AlCo}_2\text{Er}_2/\text{Al}_5\text{Co}_4\text{Er}_{11}/\lambda$	20.28	43.23	21.67	28.49	36.74	31.88
#B25	25	10	65	$\text{Al}_2\text{Er}_3/\lambda/\text{Al}_3\text{Co}_3\text{Er}_{14}$	32.83	9.97	20.3	15.40	44.11	23.52
#B26	22.5	47.5	30	$\text{Co}_{17}\text{Er}_2/\text{Co}_7\text{Er}_2$	21.78	62.06	16.36	63.04		
#B27	20	75	5	$\lambda/\text{Al}_2\text{Er}_3/\text{Al}_3\text{CoEr}_2$	21.18	13.71	37.60	7.08	53.87	15.6
#B28	20	70	10	$\text{Co}_7\text{Er}_2/\text{Co}_3\text{Er}/\text{AlCo}$	5.53	74.20	10.24	69.73	24.9	62.85
#B29	20	60	20	$\lambda/\text{AlCo}$	41.01	27.48	50.63	48.83		
#B30	20	25	55	$\text{Al}_2\text{Er}_3/\text{Al}_3\text{Co}_3\text{Er}_{14}$	37.93	5.01	20.9	10.76		
#B31	17.5	55	27.5	$\text{Al}_2\text{Er}_3/\text{Al}_3\text{Co}_3\text{Er}_{14}/\lambda$	36.31	6.51	20.11	12.69	43.84	23.69
#B32	15	70	15	$\lambda_1/\lambda_2$	41.75	26.42	41.65	34.27		
#B33	15	50	35	$\text{AlCo}_2\text{Er}/\lambda/\text{AlCo}$	21.89	53.27	22.45	45.46	47.90	50.07
#B34	15	5	80	$\text{AlCo}_2\text{Er}/\text{AlCo}/\text{Co}_3\text{Er}$	20.77	54.00	44.76	55.05	12.57	62.47

Alloys #B21 and #B24 were respectively located in the following adjacent three-phase equilibrium fields:  $\text{AlCo}_2\text{Er}_6 + \text{AlCo}_2\text{Er}_2 + \text{Al}_5\text{Co}_4\text{Er}_{11}$  and  $\text{AlCo}_2\text{Er}_2 + \text{Al}_5\text{Co}_4\text{Er}_{11} + \lambda$  (Fig. 10), with both alloys containing two same phases:  $\text{AlCo}_2\text{Er}_2$  and

$\text{Al}_5\text{Co}_4\text{Er}_{11}$ . Phase  $\text{Al}_5\text{Co}_4\text{Er}_{11}$  has not yet been reported in the literature; thus, the exact atomic ratio and the lattice parameters of the phase need further study.



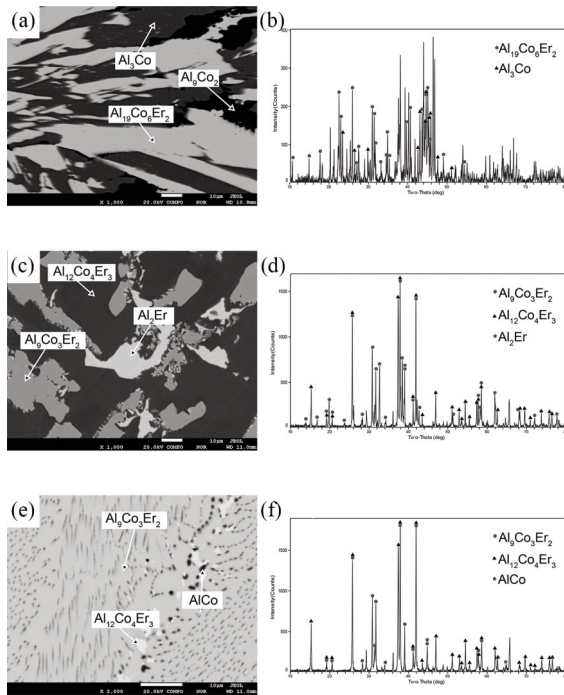


**Figure 9.** EPMA images and XRD results of 600°C-annealed alloys containing two phases after quenching: (a) microstructure of alloy #B5; (b) XRD result of alloy #B5; (c) microstructure of alloy #B14; (d) XRD result of alloy #B14; (e) microstructure of alloy #B17; (f) XRD result of alloy #B17

As shown in Fig. 11(a, c, e), one distinct three-phase field occurred in each of alloys #B25, #B27, and #B30. According to the XRD pattern analysis (Fig. 11b, d, f), alloys #B25 and #B27 were located in the following three-phase fields:  $\text{Al}_2\text{Er}_3 + \text{Al}_3\text{Co}_3\text{Er}_{14} + \lambda$  and  $\text{Al}_2\text{Er}_3 + \text{Al}_3\text{Co}_3\text{Er}_{14} + \text{Al}_3\text{CoEr}_2$ , respectively. Because of the tiny spot of the dark phase in alloy

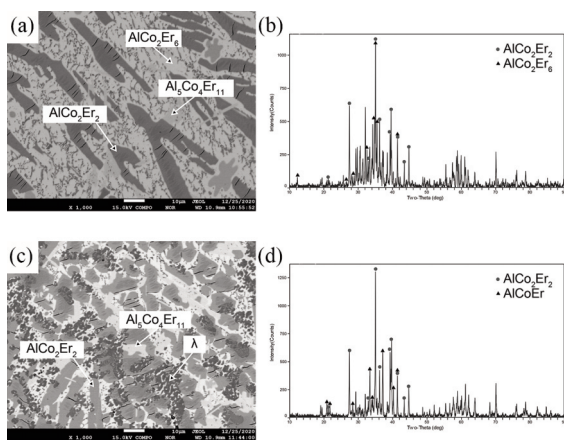


**Figure 10.** EPMA images and XRD results of 600°C-annealed alloys containing two phases after quenching: (a) microstructure of alloy #B21; (b) XRD result of alloy #B21; (c) microstructure of alloy #B24; (d) XRD result of alloy #B24

#B30, the third phase could not be confirmed, however, according to the peripheral phase regions and phase law, #B30 is assumed to be in the three-phase field  $\text{Al}_2\text{Er}_3 + \text{Al}_3\text{Co}_3\text{Er}_{14} + \text{AlEr}_2$ .

Figure 12(a) shows the three-phase microstructures of  $\text{AlCo} + \text{Co}_7\text{Er}_2 + \text{Co}_{17}\text{Er}_2$  of alloy #B22, and the XRD result is shown in Fig. 12(b). According to the SEM, EPMA, and XRD data of alloys #B28 (Fig. 12c, d) and #B34 (Fig. 12e, d), the alloys were respectively located in the  $\text{AlCo} + \text{Co}_7\text{Er}_2 + \text{Co}_3\text{Er}$  and  $\text{AlCo}_2\text{Er} + \text{AlCo} + \text{Co}_3\text{Er}$  three-phase fields.

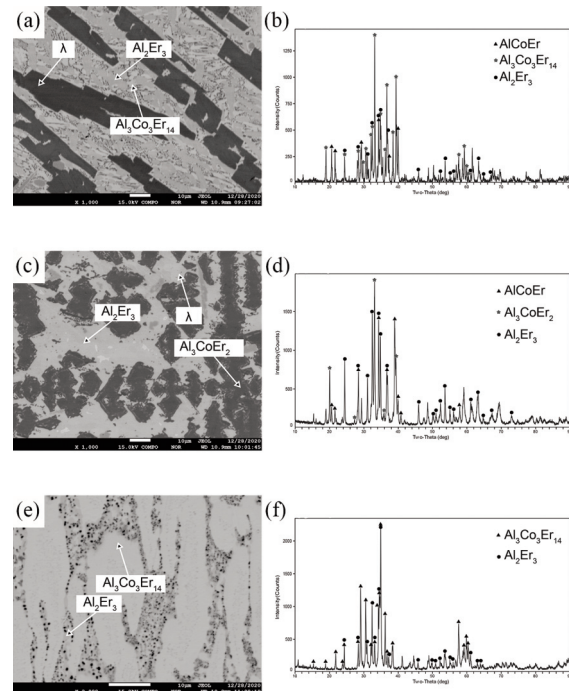


**Figure 11.** EPMA images and XRD results of 600°C-annealed alloys containing two phases after quenching: (a) microstructure of alloy #B25; (b) XRD result of alloy #B25; (c) microstructure of alloy #B27; (d) XRD result of alloy #B27; (e) microstructure of alloy #B30; (f) XRD result of alloy #B30

Based on the above analysis and the EPMA data in Table 3, the isothermal section of the Al–Co–Er ternary system at 600°C was established (Fig. 13). As shown in Fig. 13, 10 ternary intermediate compounds were detected in the Al–Co–Er system at 600°C:  $\text{Al}_{19}\text{Co}_6\text{Er}_2$ ,  $\text{Al}_9\text{Co}_3\text{Er}_2$ ,  $\text{Al}_{12}\text{Co}_4\text{Er}_3$ ,  $\lambda$  (a solid solution including  $\text{AlCoEr}$  and  $\text{Al}_4\text{Co}_2\text{Er}_3$ ),  $\text{AlCo}_2\text{Er}$ ,  $\text{Al}_3\text{CoEr}_2$ ,  $\text{AlCo}_2\text{Er}_2$ ,  $\text{AlCo}_2\text{Er}_6$ ,  $\text{Al}_3\text{Co}_3\text{Er}_{14}$ , and  $\text{Al}_5\text{Co}_4\text{Er}_{11}$ . Six of these compounds ( $\text{Al}_{19}\text{Co}_6\text{Er}_2$ ,  $\text{Al}_{12}\text{Co}_4\text{Er}_3$ ,  $\text{AlCo}_2\text{Er}$ ,  $\text{AlCo}_2\text{Er}_6$ ,  $\text{Al}_3\text{Co}_3\text{Er}_{14}$ , and  $\text{Al}_5\text{Co}_4\text{Er}_{11}$ ) have not been previously reported. The maximum solid solubilities of Al in  $\text{Co}_{17}\text{Er}_2$  and  $\text{Co}_7\text{Er}_2$  were 10.17 at.% and 10.24 at.%, respectively, whereas those of Co in  $\text{Al}_2\text{Er}$  and  $\text{Al}_2\text{Er}_3$  were 3.63 at.% and 2.01 at.%, respectively.

Moreover, the solubility range of AlCo was from 44.76 at.% Al to 50.94 at.% Al.

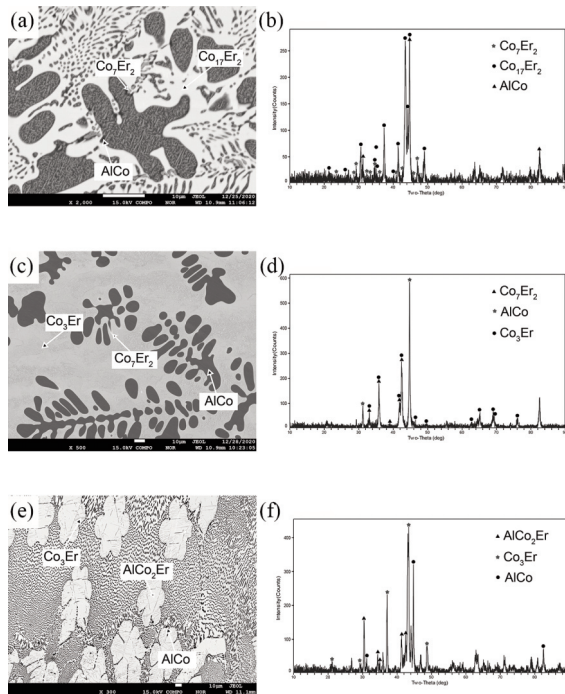


**Figure 12.** EPMA images and XRD results of 600°C-annealed alloys containing two phases after quenching: (a) microstructure of alloy #B22; (b) XRD result of alloy #B22; (c) microstructure of alloy #B28; (d) XRD result of alloy #B28; (e) microstructure of alloy #B34; (f) XRD result of alloy #B34

Through the analysis of 34 equilibrium alloy samples, 20 three-phase equilibrium fields and 6 two-phase equilibrium fields were determined: (Al)+Al<sub>3</sub>Er+Al<sub>9</sub>Co<sub>2</sub>, Al<sub>2</sub>Er+Al<sub>2</sub>Er<sub>3</sub>+AlEr, Al<sub>3</sub>Er+Al<sub>19</sub>Co<sub>6</sub>Er<sub>2</sub>+Al<sub>9</sub>Co<sub>2</sub>, Al<sub>9</sub>Co<sub>2</sub>+Al<sub>19</sub>Co<sub>6</sub>Er<sub>2</sub>+Al<sub>13</sub>Co<sub>4</sub>, Al<sub>5</sub>Co<sub>2</sub>+AlCo+Al<sub>9</sub>Co<sub>3</sub>Er<sub>2</sub>, Al<sub>9</sub>Co<sub>3</sub>Er<sub>2</sub>+Al<sub>3</sub>Er+Al<sub>2</sub>Er, Al<sub>3</sub>Er+Al<sub>19</sub>Co<sub>6</sub>Er<sub>2</sub>+Al<sub>9</sub>Co<sub>2</sub>, Al<sub>9</sub>Co<sub>3</sub>Er<sub>2</sub>+Al<sub>19</sub>Co<sub>6</sub>Er<sub>2</sub>+Al<sub>5</sub>Co<sub>2</sub>, AlCo+Al<sub>12</sub>Co<sub>4</sub>Er<sub>3</sub>+λ, Al<sub>9</sub>Co<sub>3</sub>Er<sub>2</sub>+Al<sub>19</sub>Co<sub>6</sub>Er<sub>2</sub>+Al<sub>5</sub>Co<sub>2</sub>, AlCo+Al<sub>12</sub>Co<sub>4</sub>Er<sub>3</sub>+λ, Al<sub>9</sub>Co<sub>3</sub>Er<sub>2</sub>+Al<sub>19</sub>Co<sub>6</sub>Er<sub>2</sub>+Al<sub>12</sub>Co<sub>4</sub>Er<sub>3</sub>+AlCo, Al<sub>9</sub>Co<sub>3</sub>Er<sub>2</sub>+Al<sub>12</sub>Co<sub>4</sub>Er<sub>3</sub>+Al<sub>2</sub>Er, Al<sub>9</sub>Co<sub>3</sub>Er<sub>2</sub>+Al<sub>12</sub>Co<sub>4</sub>Er<sub>3</sub>+Al<sub>2</sub>Er, Al<sub>3</sub>Co+Al<sub>19</sub>Co<sub>6</sub>Er<sub>2</sub>+Al<sub>9</sub>Co<sub>2</sub>, AlCo<sub>2</sub>Er<sub>2</sub>+AlCo<sub>2</sub>Er<sub>6</sub>+Al<sub>5</sub>Co<sub>4</sub>Er<sub>11</sub>, AlCo+Co<sub>17</sub>Er<sub>2</sub>+Co<sub>7</sub>Er<sub>2</sub>, λ+AlCo<sub>2</sub>Er<sub>2</sub>+Al<sub>5</sub>Co<sub>4</sub>Er<sub>11</sub>, λ+Al<sub>2</sub>Er<sub>3</sub>+Al<sub>3</sub>Co<sub>3</sub>Er<sub>14</sub>, Al<sub>2</sub>Er<sub>3</sub>+λ+Al<sub>3</sub>Co<sub>3</sub>Er<sub>14</sub>, AlCo+Co<sub>7</sub>Er<sub>2</sub>+Co<sub>3</sub>Er, Al<sub>2</sub>Er<sub>3</sub>+Al<sub>3</sub>Co<sub>3</sub>Er<sub>14</sub>+AlEr<sub>2</sub>, AlCo+AlCo<sub>2</sub>Er+λ, Al<sub>5</sub>Co<sub>2</sub>+Al<sub>19</sub>Co<sub>6</sub>Er<sub>2</sub>, Al<sub>12</sub>Co<sub>4</sub>Er<sub>3</sub>+Al<sub>2</sub>Er, Al<sub>2</sub>Er<sub>3</sub>+Al<sub>2</sub>Er, AlCo+Co<sub>17</sub>Er<sub>2</sub>, Co<sub>17</sub>Er<sub>2</sub>+Co<sub>7</sub>Er<sub>2</sub>, λ+AlCo.

Then, according to the extrapolation of the three binary optimized phase diagrams and the actual determination of the phase equilibrium relationship, the undetected phase fields were obtained by prediction (shown by dashed lines in Fig. 13).

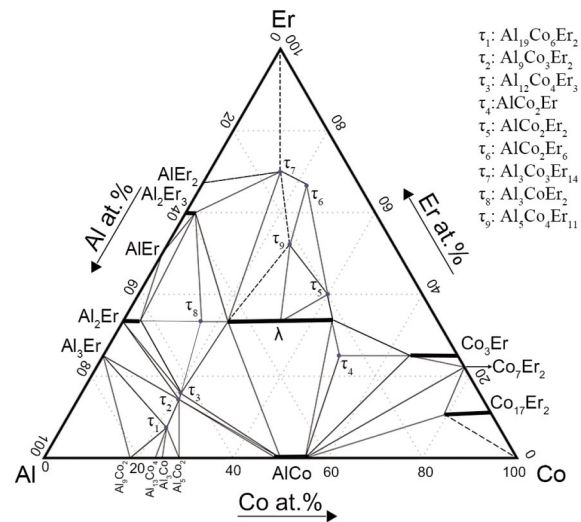


**Figure 13.** Isothermal section of Al-Co-Er system at 600°C

#### 4. Conclusions

The isothermal sections of the Al-Co-Er ternary system at 400°C and 600°C were determined via EPMA and XRD. Eight ternary intermediate compounds were detected in the Al-Co-Er system at 400°C, which included five ternary intermediate compounds that have not been reported in the literature (Al<sub>19</sub>Co<sub>6</sub>Er<sub>2</sub>, Al<sub>12</sub>Co<sub>4</sub>Er<sub>3</sub>, AlCo<sub>2</sub>Er, AlCo<sub>2</sub>Er<sub>6</sub>, and Al<sub>3</sub>Co<sub>3</sub>Er<sub>14</sub>). Furthermore, 18 three-phase equilibrium regions and 6 two-phase equilibrium regions were detected in the isothermal section of the Al-Co-Er system at 400°C. Ten ternary intermediate compounds were detected in the Al-Co-Er system at 600°C, among which six have not been reported in the literature (Al<sub>19</sub>Co<sub>6</sub>Er<sub>2</sub>, Al<sub>12</sub>Co<sub>4</sub>Er<sub>3</sub>, AlCo<sub>2</sub>Er, AlCo<sub>2</sub>Er<sub>6</sub>, Al<sub>3</sub>Co<sub>3</sub>Er<sub>14</sub>, and Al<sub>5</sub>Co<sub>4</sub>Er<sub>11</sub>). In addition, 20 three-phase equilibrium fields and 6 two-phase equilibrium fields were determined in the isothermal section of the Al-Co-Er system at 600°C. The solution range of the solid solution phase λ was confirmed to be from 22.22 at.% Al to 44.44 at.% Al.

#### Acknowledgments

The work was financially supported by National Natural Science Foundation of China (Grant No. 51871248), and Natural Science Foundation of Hunan Province, China (Grant No. 2020JJ4739).

#### References

- [1] A. Wilm, Metall. Z. Gesamte Hüttenkunde, 8 (1911) 225–227.
- [2] E. Hornbogen, J. Light Met., 1 (2) (2001) 127–132.
- [3] Q.N. Gao, J. Wang, Y. Du, S.L. Shang, Z.K. Liu, Y.J. Liu, J. Min. Metall. Sect. B-Metall., 57(1) (2021) 31–40.



- [4] J. Sxhiozt, K. W. Jacobsen, Science, 301 (5638) (2003) 1357-1359.
- [5] T. Dursun, C. Soutis, Mater. Des., 56 (4) (2014) 862-871.
- [6] J. H. Chen, E. Costan, M. A. van Huis, Q. Xu, H. W. Zandbergen. Science, 312 (5772) (2006) 416-419.
- [7] J. H. Martin, B. D. Yahata, J. M. Hundley, J. A. Mayer, T. A. Schaedler, T. M. Pollock, Nature, 549 (7672) (2017) 365-369.
- [8] Z. Wang, R. T. Qu, S. Scudino, B. A. Sun, K. G. Prashanth, D. V. Louzguine-Luzgin, M. W. Chen, Z. F. Zhang, J. Eckert, NPG Asia Mater., 7 (12) (2015) e229.
- [9] A. Inoue, Prog. Mater Sci., 43 (5) (1998) 365-520.
- [10] N. C. Wu, L. Zuo, J. Q. Wang, E. Ma, Acta Mater., 108 (2016) 143-151.
- [11] K. G. Prashanth, H. S. Shahabi, H. Attar, V. C. Srivastava, N. Ellendt, V. Uhlenwinkel, J. Eckert, S. Scudino, Addit. Manuf., 6 (2015) 1-5.
- [12] P. Riani, R. Freccero, K. Sufryd, L. Arrighi, G. Cacciamani, J. Phase Equilib. Diff., 41 (2020) 347-364.
- [13] Z. Zhang, Y. Li, H. Li, D. Zhang, Z. Zhao, Q. Du, J. Zhang, Calphad, 74 (2021) 102298.
- [14] M. Noori, B. Hallstedt, Calphad, 71 (2020) 101793.
- [15] D. Huang, S. Liu, Y. Du, Calphad, 68(2020) 101693.
- [16] F. Kozina, Z. Zovko Brodarac, M. Petric, A. Penko, J. Min. Metall. Sect. B-Metall., 56(3) (2020) 425-433.
- [17] L. Guillet, Le Génie Civil, 41(1902) 169-172.
- [18] A. G. C. Gwyer, Z. Anorg. Chem., 57 (1908) 113-153.
- [19] L. A. Panteleimonov, E. B. Badtiev, L. V. Aleshina, Moscow Univ. Chem. Bull., 29 (1974) 91-92.
- [20] A. J. Mcalister, Bull. Alloy Phase Diagr., 10 (1989) 646-650.
- [21] F. Stein, C. He, N. Dupin, Intermetallics, 39 (2013) 58-68.
- [22] N. Dupin, I. Ansara, Rev Metall, 95 (1998) 1121-1129.
- [23] K. H. J. Buschow, J. H. N. van Vucht, Z. Metallkd., 56 (1965) 9-13.
- [24] G. Cacciamani, A. Saccone, S. De Negri, R. Ferro, J. Phase Equilib., 23 (1) (2002) 38-50.
- [25] K. H. J. Buschow, Philips Res. Rep., 26 (1971) 49-64.
- [26] H. Okamoto, J. Phase Equilib., 17 (4) (1996) 368-368.
- [27] C. H. Wu, Z. Metallkd., 84 (1993) 170-173.
- [28] H. Okamoto, T. B. Massalski, J. Phase Equilib., 14 (3) (1993) 316-339.
- [29] C. P. Wang, A. Q. Zheng, X. J. Liu, K. Ishida, J. Alloys Compd., 478 (2009) 197-201.
- [30] P. Villars, Pearson's Handbook, ASM International, Metals Park, Ohio, 1997.
- [31] H. Oesterreicher, J. Less-Common Met., 33 (1973) 25-41.
- [32] H. Oesterreicher, W. E. Wallace, J. Less-Common Met., 13 (1) (1967) 91-102.
- [33] C. Routsis, J. K. Yakinthos, J. Alloys Compd., 323-324 (0) (2001) 427-430.
- [34] M. Pani, F. Merlo, M. L. Fornasini, Z. Kristallogr., 217 (7-8) (2002) 415-419.
- [35] A. M. B. Douglas, Acta Crystallogr., 3 (1950) 19-24.
- [36] T. B. Massalski, Binary Phase Diagram (2nd edition), ASM International, Metals Park, Ohio, 1990.
- [37] P. S. Wang, W. Xiong, U. R. Katner, C. E. Campbell, E. A. Lass, O. Y. Kontsevoi, G. B. Olson, Calphad, 59 (2017) 112-130.
- [38] W. He, L. H. Tang, L. Yang, J. X. Wen, L. M. Zeng, J. Alloys Compd., 491 (1-2) (2010) 149-152.
- [39] Y. H. Zhuang, X. Chen, J. L. Yan, J. Alloys Compd., 465 (1-2) (2008) 183-185.
- [40] B. Kotur, O. Myakush, I. Zavaliy, J. Alloys Compd., 442 (1-2) (2007) 17-21.
- [41] R. V. Skolozdra, Y. S. Mudryk, L. P. Romaka, J. Alloys Compd., 296 (1-2) (2000) 290-292.
- [42] W. He, Y. Z. Zhang, Y. H. Zhao, L. M. Zeng, J. Alloys Compd., 509 (5) (2011) 1590-1594.
- [43] L. G. Zhang, L. B. Liu, G. X. Huang, H. Y. Qi, B. R. Jia, Z. P. Jin, Calphad, 32 (3) (2008) 527-534.
- [44] G. X. Huang, L. B. Liu, L. G. Zhang, Z. P. Jin, J. Min. Metall. Sect. B., 52 (2) (2016) 177-183.
- [45] H. Bo, L. B. Liu, Z. P. Jin, J. Alloys Compd., 490 (1-2) (2010) 318-325.

## FAZNE RAVNOTEŽE U Al-Co-Er SISTEMU NA 400°C I NA 600°C

L.-H. Zheng, L.-G. Zhang \*, F.-Y. Zhao, L.-B. Liu, D. Wang, C.-J. Wu

Fakultet za nauku o materijalima i inženjerstvo, Centralno - južni univerzitet, Čangša, Kina

### Apstrakt

Izotermalni preseki Al-Co-Er sistema na 400°C i na 600°C ispitivani su pomoću rentgenske difrakcije (XRD), skenirajućeg elektronskog mikroskopa (SEM), i tehnikama elektronske mikroanalize (EPMA). U izotermalnom preseku na 400°C identifikovano je 18 trofaznih područja. Maksimalna rastvorljivost Al u  $Co_3Er$ , i  $Co_2Er$  fazama bila je 13.93 at.% i 16.13 at.%. Maksimalna rastvorljivost Co u  $Al_2Er$ ,  $Al_2Er_3$ , i  $AlEr_2$  fazama bila je 6.93 at.%, 6.65 at.%, i 6.49 at.%, pojedinačno. Područje čvrstog rastvora  $\lambda$  je od 22.22 at.% Al do 44.44 at.% Al, dok je izotermalni presek na 600°C uključivao 20 trofaznih polja. Maksimalna rastvorljivost Al u  $Co_{17}Er_2$ , i  $Co_7Er_2$  fazama bila je 10.17 at.% i 10.24 at.%, pojedinačno, dok je maksimalna rastvorljivost Co u  $Al_2Er$  i  $Al_2Er_3$  fazama bila 3.63 at.% i 2.01 at.%, pojedinačno.

**Ključne reči:** Fazne ravnoteže; Al-Co-Er; Legure aluminijuma

